Improving the lifetime of aluminum-based superconducting qubits through atomic layer etching and deposition

Neha Mahuli,* Joaquin Minguzzi, Jiansong Gao, Rachel Resnick,† Sandra Diez,‡ Cosmic Raj, Guillaume Marcaud, Matthew Hunt, Loren Swenson, Jefferson Rose, Oskar Painter, and Ignace Jarrige§
AWS Center for Quantum Computing, Pasadena, CA 91106, USA
(Dated: June 18, 2025)

We present a dry surface treatment combining atomic layer etching and deposition (ALE and ALD) to mitigate dielectric loss in fully fabricated superconducting quantum devices formed from aluminum thin films on silicon. The treatment, performed as a final processing step prior to device packaging, starts by conformally removing the native metal oxide and fabrication residues from the exposed surfaces through ALE before *in situ* encapsulating the metal surfaces with a thin dielectric layer using ALD. We measure a two-fold reduction in loss attributed to two-level system (TLS) absorption in treated aluminum-based resonators and planar transmon qubits. Treated transmons with compact capacitor plates and gaps achieve median Q and T_1 values of $3.7 \pm 0.4 \times 10^6$ and 200 ± 20 μs, respectively. These improvements were found to be sustained over several months. We discuss how the combination of ALE and ALD reverses fabrication-induced surface damages to significantly and durably improve device performance via a reduction of the TLS defect density in the capacitive elements.

I. INTRODUCTION

Superconducting transmons are a leading platform for building a scalable, fault-tolerant quantum computer capable of solving problems currently intractable with classical computing architecture[1]. In the early stages of development, transmon performance improved primarily through design optimizations, such as reducing dielectric participation in critical surfaces[2–4] and enhancing readout via Purcell filtering[5,6]. More recently, the focus has shifted toward enhancing the quality of materials, a strategy that has already shown great promise in mitigating two-level system (TLS) losses and improving transmon energy-relaxation times[7–9].

Among the main dielectric regions in superconducting circuits, the metal-air (MA) and substrate-air (SA) interfaces are particularly susceptible to degradation during the fabrication process. These interfaces are often characterized by polymeric residues, interstitial contaminants, morphological damage, and thickened oxide layers, resulting in a larger loss tangent compared to other interfaces[10]. This stresses the need to develop post-fabrication surface treatment methods that alleviate or eliminate these effects without introducing new damage.

Recent efforts to reduce dielectric loss at the MA interface have centered on three primary approaches: (i) exploring new ground-layer materials that form low-loss native oxides[8], (ii) chemically etching defect-rich surface layers[11–14], and (iii) capping the top surface of the ground layer with a lower-loss superconductor, or a noble metal to prevent oxidation[15–18]. In (iii), surface capping was performed on the blanket ground layer prior to fabrication, as subsequent etching exposed the sidewalls of the superconductor. As a result, amorphous oxides and process-induced defects on the sidewalls likely dominated the dielectric loss in these capped devices[18]. Here, we present an alternative surface engineering approach that overcomes this limitation by treating all exposed surfaces of fully fabricated devices using a combination of atomic layer etching and deposition (ALE and ALD) as a final surface modification step prior to device packaging.

Both ALE and ALD rely on a self-limiting, sequential gas-phase surface reaction mechanism to respectively remove and form material layers with monolayer precision and a high conformality compatible with three-dimensional structures. By applying these techniques to aluminum (Al)-based coplanar waveguide (CPW) resonators and planar transmons, we show that fabrication-related contamination of the Al and silicon (Si) substrate surfaces is substantially reduced and the lossy native Al oxide layer is selectively replaced with a thin and stoichiometric Al_2O_3 capping layer. These modifications to the MA and SA interfaces correlate with a 50% reduction in dielectric loss in the resonators and a two-fold increase in both the transmon median quality factor (Q) and energy relaxation times (T_1), reaching median Q and T_1 values of $3.69 \pm 0.42 \times 10^6$ and 196 ± 22 μs, respectively. These improvements are achieved for several fabricated chips, and across a frequency range spanning 2.2-4.4 GHz. This study shows that the *in situ* combination of ALE and ALD serves as an effective and scalable surface engineering strategy for Al-on-Si superconducting quantum circuits, with potential applications across a myriad of architectures and materials.

II. RESULTS AND DISCUSSION

A. Surface Engineering Effects on Resonator Loss Tangent

Superconducting microwave resonators provide an effective platform for evaluating materials-induced dielectric loss, minimizing the design, fabrication, and measurement overhead compared to transmons[19,20]. $\lambda/4$-CPW resonators were fabricated using 100-nm thick Al

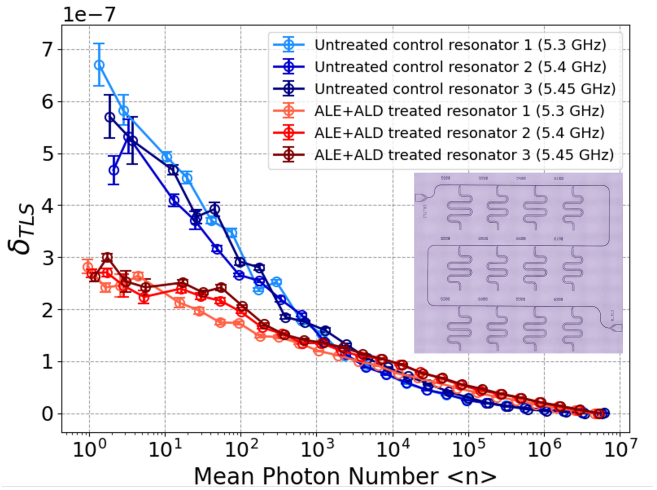

FIG. 1. δ_{TLS} as a function of power for three representative resonators, comparing untreated and ALE+ALD treated chips. Inset: Micrograph of a CPW resonator chip.

films on high-resistivity ($> 20\,\mathrm{k\Omega \cdot cm}$) silicon substrates, with trace and gap widths of 30 μm each. Each chip contains 12 resonators with frequencies ranging from 5.2 to 6.2 GHz, inductively coupled to the transmission line, as shown in the inset of Figure 1. We performed S_{21} transmission measurements in a dilution refrigerator at a base temperature of 10 mK and the intrinsic quality factors (Q_i) were extracted using a circle-fitting method[21,22]. Measurements were conducted on untreated devices to establish a baseline, and directly compared with ALE+ALD treated devices.

Our devices exhibit the typical saturation behavior of Q_i as a function of photon number. In the single-photon limit, losses are dominated by unsaturated or partially saturated TLSs, while at higher power levels, Q_i is predominantly limited by other loss mechanisms such as vortices, non-equilibrium quasi-particles, or packaging modes. We quantify the TLS contribution to loss, δ_{TLS}, from high-power (HP) and low-power (LP) Q_i per the following equation[23]:

$$\delta_{\mathrm{TLS}} = \frac{1}{Q_{\mathrm{TLS}}} = \frac{1}{Q_i^{\mathrm{LP}}} - \frac{1}{Q_i^{\mathrm{HP}}} \tag{1}$$

Figure 1 shows a power sweep of δ_{TLS} for three untreated/treated pairs of representative resonators at 5.3, 5.4 and 5.45 GHz frequencies. At single-photon powers, the loss of the ALE+ALD treated resonators is approximately half that of the untreated resonators. This shows that materials-based losses can be efficiently reduced in single-layer Al devices using the ALE+ALD treatment.

B. Surface Engineering Effects on Transmon Performance

Motivated by the promising resonator results, we extend our study to transmons made from Al on Si. Here, we compare the transmon qubit energy relaxation time (T_1), and corresponding effective quality factor (Q), before and after the treatment. The measurements were conducted on Josephson junction (JJ) based planar transmons coupled to CPW readout resonators. Five chips, each containing four tunable transmons with variable-size junctions and constant-geometry shunt capacitors (24-μm in-plane dimension, 30-μm gap-to-ground plane), were measured in the frequency range of 2.2–4.4 GHz before and after the treatment. Further qubit design details and a micrograph of a representative transmon device are provided in Figure SI-1 of the Supplementary Information (SI). To improve the pre-treatment statistical analysis, six additional untreated chips were measured. One chip was also measured before and after annealing at 300°C under vacuum in the ALD chamber to disentangle the impact of heating from the ALE+ALD treatment, which also takes place at 300°C. Transmon and readout resonator frequencies were measured, and qubit T_1-time data collected over several hours across a broad frequency range. This approach enabled us to sample a wider distribution of possible TLS defects, facilitating faster and more accurate characterization of the T_1 distribution[24,25]. Based on the standard tunneling model (STM)[26], it can be approximated that the TLS density remains constant across the measured frequency range, suggesting a frequency-independent metric of transmon"quality" based on the effective quality factor $Q = 2\pi f_{01} T_1$ [4], where f_{01} is the ground-to-first excited state transition frequency of the transmon.

T_1 and Q measurements of treated and untreated transmons are presented in Figure 2(a) and (b), respectively. Across the measured frequency range, median Q values remain mainly under 3×10^6 for the untreated control and annealed-only devices and increase to 3-7×10^6 after the treatment, with some values exceeding the 9×10^6 mark. Similarly, most median T_1 times for the untreated and annealed-only devices are below 150 μs, whereas treated devices achieve median T_1 values in the 150–400 μs range. These results highlight the effectiveness of the ALE+ALD treatment in reducing the TLS losses in planar transmon devices, consistent with earlier observations from single layer resonators.

This improvement can be further quantified by comparing the pre- and post-treatment empirical probability density function (e-PDF) and cumulative distribution function (e-CDF) of a frequency-independent parameter, Q, shown in Figure 2(c). Prior to the treatment, the e-PDF exhibits a median Q of $1.91 \pm 0.18 \times 10^6$, while the e-CDF shows a 90$^{\mathrm{th}}$-percentile of 2.67×10^6, which corresponds to a median T_1 of 101 ± 10 μs and a 90$^{\mathrm{th}}$-percentile T_1 of 142 μs for f_{01} of 3 GHz. Following the treatment, the median Q in the e-PDF increases to $3.69 \pm 0.42 \times 10^6$, while the 90$^{\mathrm{th}}$-percentile Q in the e-CDF rises to 5.9×10^6, corresponding to a median T_1 of 196 ± 22 μs and 90$^{\mathrm{th}}$-percentile T_1 of 313 μs for f_{01} of 3 GHz. While this enhancement reflects a reduction in TLS density after treatment, the T_1 floor remains largely unchanged, likely

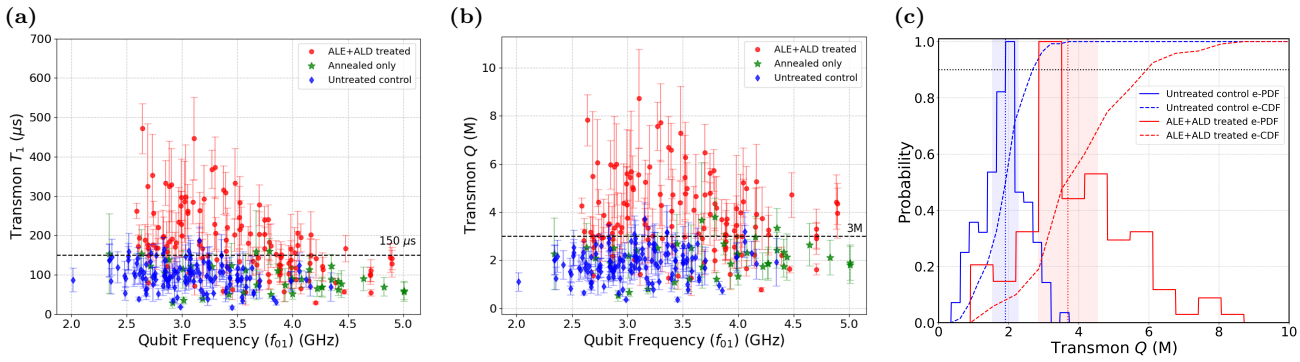

FIG. 2. Frequency dependence of (a) measured T_1 times and (b) estimated Q for various devices: untreated, ALE+ALD treated, and annealed-only. The dashed lines are a guide to the eye. (c) The empirical probability distribution function (e-PDF) and cumulative distribution function (e-CDF) are also shown for Q before and after the treatment; the dotted horizontal line, vertical lines and shaded areas represent the 90$^{\text{th}}$-percentile, median, and median absolute deviation (MAD), respectively.

due to the finite residual population of more strongly coupled TLSs still present on the capacitor pads. As a result, the spread in T_1 and Q values increases, leading to a higher standard deviation after treatment.

The highest performing treated devices are consistently observed within the 2.6–3.7 GHz range, with some of the Q values surpassing 6×10^6. Purcell loss due to radiation into the qubit read-out resonator, illustrated in Figure SI-2, is presumed to contribute to the reduction in T_1 and Q at higher frequencies. Regardless of the Purcell effect, the consistent enhancement in T_1 and Q post-ALE+ALD treatment across the studied frequency range, which is not achieved by annealing alone, provides compelling evidence that the surface dielectric loss of the transmons is reduced by the ALE+ALD treatment specifically. No decline in T_1 and Q was observed in transmons measured over periods of up to 8-9 months after the treatment, highlighting the long-term stability of this treatment for Al-on-Si based superconducting quantum circuits.

Additionally, a consistent increase in transmon frequency (f_{01}) by several hundreds of MHz was also observed for all treated transmons (as shown in Figure SI-3). This increase originates from junction evolution, as we observe a rise in junction energy (E_j) after the treatment, while capacitive energy (E_c) remains unaffected. This frequency shift results from the elevated processing temperatures during treatment, which was also confirmed with annealed-only devices; however, its absolute magnitude is likely influenced by additional factors, such as the initial interface quality before the JJ deposition and fabrication variability. Additionally, we observe that transmon Q decreases with increasing frequency shift (as shown in Figure SI-4), likely due to enhanced Purcell loss as f_{01} approaches the readout frequency.

C. Surface Chemistry

The ALE chemistry, utilizing alternating exposures of trimethylaluminum (TMA) and hydrogen fluoride-pyridine (HF-pyridine) at 300°C[27], was developed to etch the native aluminum oxide. The subsequent ALD process, using TMA and water (H_2O)[28], was tuned to regrow a 1-nm thick Al_2O_3 layer. Detailed process parameters and methodology are provided in the Methods section. Here, we characterize the effect of these processes on the chemical properties of the surface of our devices, using a combination of X-ray photoelectron spectroscopy (XPS), photo-induced force infrared microscopy (PiFM), and transmission electron microscopy complemented by electron energy loss spectroscopy (TEM-EELS). Using lab-scale XPS with an Al Kα X-ray source (1486.6 eV), we measured the Al 2p, C 1s, and O 1s core levels on the surface of transmon qubit chips. A detailed description of the fitting procedure is provided in SI (Figures SI-5 through 7). To check the consistency of the observed trends, we measured two sites per untreated and annealed-only chip, and a total of four sites on two different treated chips.

The XPS data is shown in Figure 3 for the surfaces of untreated, annealed-only, and ALE+ALD treated transmon qubit chips, and compared with blanket films of ALD-grown Al_2O_3 and evaporated Al. In the fits, up to four characteristic binding energies (BE) can be distinguished for the Al 2p oxide components. Ranked by increasing BE (see Figure 3(a)), these are assigned to native Al oxide, ALD-grown Al_2O_3, post-fabrication AlO_x, and an aluminum oxyhydroxide phase (Al-O-OH). The differences in BE (see table in Figure 3(b)) were found to be consistent across the measured chips and sites. The higher BE of the oxide components for the untreated and annealed-only devices suggests the formation of an oxygen-rich aluminum oxide on their surface[29–31]. Additionally, the untreated chip shows a relatively strong Al-O-OH component, which is commonly found on surfaces

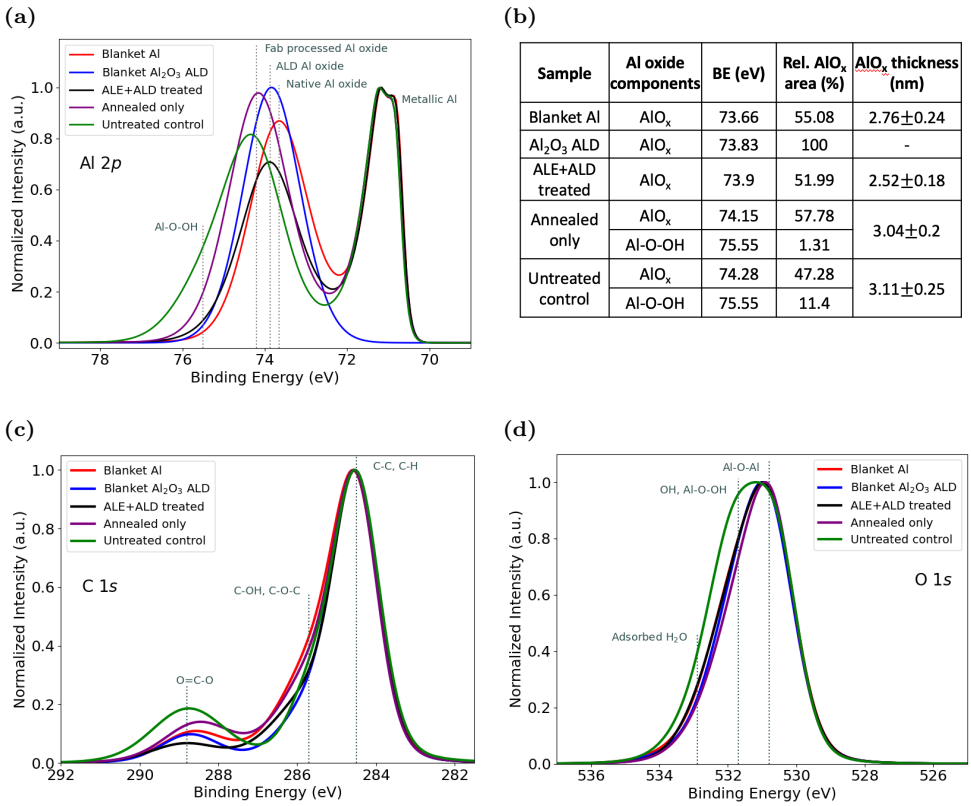

Sample	Al oxide components	BE (eV)	Rel. AlO_x area (%)	AlO_x thickness (nm)
Blanket Al	AlO_x	73.66	55.08	2.76±0.24
Al_2O_3 ALD	AlO_x	73.83	100	-
ALE+ALD treated	AlO_x	73.9	51.99	2.52±0.18
Annealed only	AlO_x	74.15	57.78	3.04±0.2
	Al-O-OH	75.55	1.31	
Untreated control	AlO_x	74.28	47.28	3.11±0.25
	Al-O-OH	75.55	11.4	

FIG. 3. (a) Al $2p$, (c) C $1s$, and (d) O $1s$ core-level XPS spectra measured on reference blanket films and transmon qubit chips. The spectra in (a) are aligned in energy and normalized in intensity to the metallic Al $2p_{3/2}$ peak at $\sim$ 70.8 eV, and in (c) and (d) they are calibrated to the C-C bonding feature at 284.5 eV. Dashed lines highlight the different oxidation states and chemical bonds inferred from the relative energy shifts. Information inferred from the deconvolution of the experimental Al $2p$ spectra is summarized in the table shown in (b).

subjected to wet chemical treatments. Annealing removes most of those Al-O-OH groups, while ALE+ALD removes all of them. Furthermore, we find that the ALE+ALD-treated Al surface has the thinnest oxide layer (2.52 ± 0.18 nm), followed by the native oxide of the Al blanket film (2.76 ± 0.24 nm), and then the untreated and annealed-only (3.1 ± 0.25 nm) chips. The thinning of the surface oxide layer of Al after ALE+ALD was confirmed by TEM-EELS, see Figure SI-8(a-d). The fact that the surface oxide in the ALE+ALD treated chip is thicker than the anticipated 1-nm thick ALD-grown layer can be attributed to the partial regrowth of a native oxide layer during the 20 seconds that the sample spends at 300°C in the 6-7 Torr atmosphere of the process chamber upon completion of the ALE step and prior to the start of the ALD process[32].

The deconvolution of the C $1s$ core level reveals three distinct chemical environments of carbon, which, in order of increasing BE, are: adventitious carbon or C-C bonding, C-OH or C-O-C bonding, and O=C-O bonding. The reduced intensity of the O=C-O bonding component after annealing, but especially after ALE+ALD where it is even weaker than in blanket Al, points to a reduction of organic species primarily stemming from residual resist contamination. The clear broadening of the O $1s$ peak observed in the untreated chip surface can be assigned to a contribution from adsorbed hydroxyl species such as Al-O-OH or $Al(OH)_3$ around 531.7 eV and adsorbed H_2O near 533 eV. These features are not observed after annealing or ALE+ALD treatment, which is consistent with the Al $2p$ data. Taken together, the XPS data shows that the ALE+ALD treatment results in a thinner and stoichiometric surface layer of Al_2O_3 with minimal polymeric contamination.

In order to gain spatially-resolved insights into this surface modification, we used PiFM to collect infrared spectroscopic data in the 800-1800 cm^{-1} range with a $\sim$10 nm lateral resolution. Areas of a few μm^2 centered around a junction and a portion of the Al/Si sidewall from a readout resonator were measured on untreated and ALE+ALD treated qubit chips. To introduce the spectroscopic features detected on the surface of our samples, Figure 4 shows the PiFM spectra averaged over the Si and Al regions, with each spectrum obtained by averaging 20-30 individual scans across the measured areas. The spectra are area-normalized to account for differences in absolute intensity and enable a more direct comparison of spectral features between the two samples.

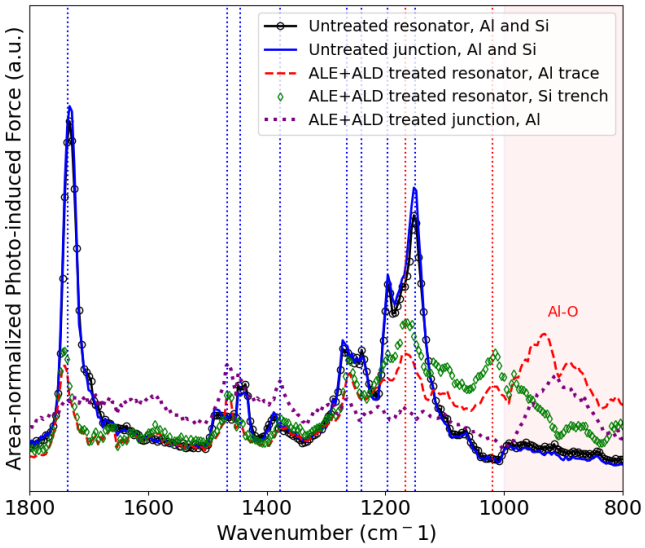

FIG. 4. Comparison of area-normalized PiFM spectra averaged across Si and Al regions measured on the untreated and ALE+ALD-treated transmon qubit chips. Dashed lines indicate characteristic peaks: blue for those present before and after the treatment, red for peaks that emerged after the treatment, and red shaded area represents the broad Al-O stretching vibration appearing only after the ALE+ALD treatment.

Dashed lines serve as visual guides for the wavenumbers of peaks present either before and after the treatment (blue) or only after the treatment (red), respectively. A detailed peak assignment is provided in Table 1 in the SI. In the untreated chip, the signal measured across all areas is dominated by spectral features assigned to poly(methyl methacrylate) (PMMA, blue dashed lines in Figure 4)[33,34], which is a resist used during liftoff and dicing steps of our fabrication flow. Despite soaking the chips in a heated solution of N-methyl pyrrolidone (NMP) followed by an acetone and isopropyl alcohol rinse to strip the PMMA, the absence of a signal from AlO_x suggests that sufficient residual PMMA remains to form a continuous layer of at least ∼2 nm thickness on the untreated surface. This lower bound on the residual PMMA thickness is derived from tests conducted to estimate the minimum thickness of a thin polymer layer that can effectively shield the infrared signal from the underlying sample.

Conversely, we observe a broad absorbance feature around 850-1000 cm^{-1} assigned to Al-O stretching vibrations[35,36] on both the resonator and junction areas of the ALE+ALD treated chip as shown by the shaded area in Figure 4. A peak corresponding to C-O stretching vibrations also appears at 1020 cm^{-1} (red dashed line) in the resonator area, suggesting PMMA decomposition. Previous studies showed that, at elevated temperatures, PMMA degrades into its monomer, MMA, which shares similar infrared features and can further undergo random scission around 300°C, breaking ester bonds into smaller fragments like C–O[37,38]. Additionally, we find that the characteristic PMMA absorbance features are weaker in the resonator area and nearly suppressed in the junction area, indicating a significant reduction in the overall PMMA contamination. The fact that the junction surface is cleaner can be attributed to the fewer exposures of the junction to MMA- and PMMA-containing resists compared to the ground plane, resulting in a thinner contamination layer and a more effective removal. Alongside these changes, a new peak appears near 1170 cm^{-1} (red dashed line), attributed to C-H bending vibrations from Al-CH_3 bonds. Such features have been previously reported during the ALD or ALE reactions involving TMA as one of the precursors[35,39–41]. Additionally, the selectivity of the Al_2O_3 growth in the nucleation regime is highly dependent on the functionalization of the starting surface, particularly for Si[42–44]. This can explain the absence of a feature corresponding to Al-O stretching in the 850-1000 cm^{-1} range in the Si trench area, which suggests that no Al_2O_3 is formed on the Si surface. The absence of Al_2O_3 on the Si surface following the ALE+ALD treatment is further confirmed by the TEM-EELS maps shown in Figure SI-8(e).

The effectiveness of the ALE+ALD treatment in reducing PMMA contamination on both Al and Si surfaces despite the intended selectivity of our ALE chemistry for AlO_x may seem surprising. The strong adhesion of PMMA to aluminum and silicon oxides has been previously attributed to the bonding between PMMA and the surface hydroxyl groups[45,46]. The annealing-induced removal of hydroxyl bonds, suggested by the Al 2p and O 1s XPS data for the annealed-only chips, is expected to substantially weaken the adhesion of PMMA to both Al and Si surfaces, making it easier for the HF used in the ALE chemistry to indiscriminately etch the PMMA away. The degradation of PMMA at the ALE process temperature (300°C)[47], as described above, is also anticipated to ease the etch.

Chemical maps were measured to gain detailed insight into the spatial uniformity of our surface treatment. Figures 5(a) and (b) present PiFM maps for untreated and treated resonator area, respectively. They were measured at 912 cm^{-1}, corresponding to the Al–O stretching vibration, and normalized by the map measured at 1740 cm^{-1}, associated with the C=O stretching vibration in PMMA. This normalization reduces local variations of the gap-field enhancement from topographic effects[48], which are considered to be constant across the measured spectral range, thereby enhancing imaging contrast based on the local ratio of Al oxide to PMMA. The raw maps are shown in Figure SI-9. The signal at 912 cm^{-1} is barely visible in the map of the untreated surface, consistent with a uniform coverage of the aluminum oxide by PMMA. After treatment, the surface shows a stronger Al-O signal across the entire Al surface. This indicates a uniform thinning of the PMMA residues revealing the aluminum oxide underneath.

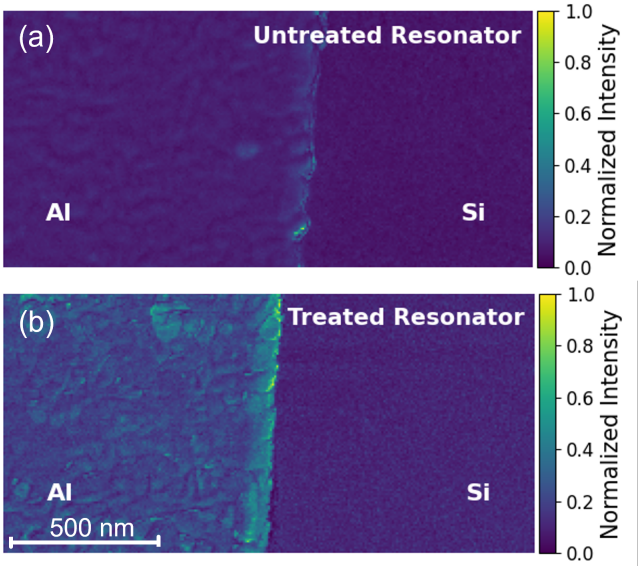

FIG. 5. (a) and (b) PiFM maps measured at 912 cm^{-1} (characteristic of Al-O) normalized by the map measured at 1740 cm^{-1} (characteristic of PMMA), for untreated and treated resonator areas, respectively.

D. Discussion

We showed that post-fabrication ALE+ALD can improve resonator and transmon performance by treating both top and sidewall surfaces, and provide compatibility with Al unlike conventional wet chemical treatments like buffered oxide etchant (BOE) or triacid[11,12,49]. We find that ALE+ALD treated surfaces exhibit a reduction in polymeric residues, along with a more stoichiometric Al native oxide. While our study does not disentangle the individual contributions of polymeric residue removal and Al oxide layer modification, it establishes a direct correlation between improved material quality at the MA and SA interfaces and increased resonator Q and transmon T_1. The comparable improvement observed in both the resonator and transmon Q further suggests that the weakly coupled TLS defects located on the surfaces of the capacitor pads limit the lifetime of our transmon qubits.

Our findings also suggest pathways for future optimization of our process. These include incorporating a step in the ALE process to remove the silicon oxide from the substrate surface, gaining a deeper understanding of the mechanism by which ALE etches organic contamination to further enhance process efficiency, and exploring lower-loss dielectric coatings beyond Al_2O_3. Finally, we find that changes in the junction also occur during the ALE/ALD process, which can lead to large shifts in the junction resistance; further studies are necessary to understand both the mechanism for, or source of, the resistance change, and the intrinsic variability of the change.

III. CONCLUSION

We have demonstrated that the energy-relaxation times of Al transmons can be systematically and durably increased by more than two-fold using a combination of ALE and ALD. These processes uniquely enable post-fabrication surface treatment by removing fabrication residues from all exposed surfaces and replacing the Al native oxide from the top surface and sidewalls with a conformal, stoichiometric Al_2O_3 layer. Another differentiator of this approach from other surface treatments is the full compatibility with Al, a rarity among commonly used native oxide etchants. The concurrent doubling of the quality factor in Al-based resonators and transmons subjected to the same ALE+ALD treatment suggests that the observed improvement primarily stems from a reduction in the density of coherence-limiting TLS defects located on the surface of the capacitor pads. These findings establish a clear correlation between TLS loss, transmon relaxation times, and the chemical composition and purity of the MA and SA interfaces. They also provide a framework for continued improvements in quantum device performance through controlled, conformal, and Al-compatible surface treatments.

IV. METHODS

A. Surface Treatment: ALE and ALD process

The ALE chemistry developed for this work relies on alternating exposures of HF-pyridine and TMA at 300°C resulting in an etch rate of 0.5 Å/cycle[27]. The reaction mechanism for the ALE of Al_2O_3 is depicted in Figure 6(a). The proposed two-half cycle reaction can be written as follows:

$$Al_2O_3^* + 6HF(g) \rightarrow 2AlF_3^* + 3H_2O(g) \uparrow \quad (2)$$

$$2AlF_3^* + 4Al(CH_3)_3(g) \rightarrow 6AlF(CH_3)_2(g) \uparrow \quad (3)$$

where the asterisk (*) denotes the surface species at the end of each half-cycle. In this ALE chemistry, HF reacts with the top few monolayers of Al_2O_3 to form AlF_3 in the first half cycle 'A' (equation (2)). In the second half cycles 'B' (equation (3)), AlF_3 is subsequently removed from the surface as $AlF(CH_3)_2$, a volatile species at 300°C, when reacted with TMA. Repetition of ABAB.. half cycles leads to the layer-by-layer etching.

Following the successful removal of the native Al oxide, the surface is encapsulated *in situ* with a thin layer of Al_2O_3 via ALD. The Al_2O_3 ALD process involves alternating exposures of TMA and water (H_2O)[28] at the same temperature of 300°C, resulting in a growth rate of 1 Å/cycle. This process begins immediately after the ALE to minimize spontaneous re-oxidation of the underlying Al surface. The reaction mechanism for the ALD of

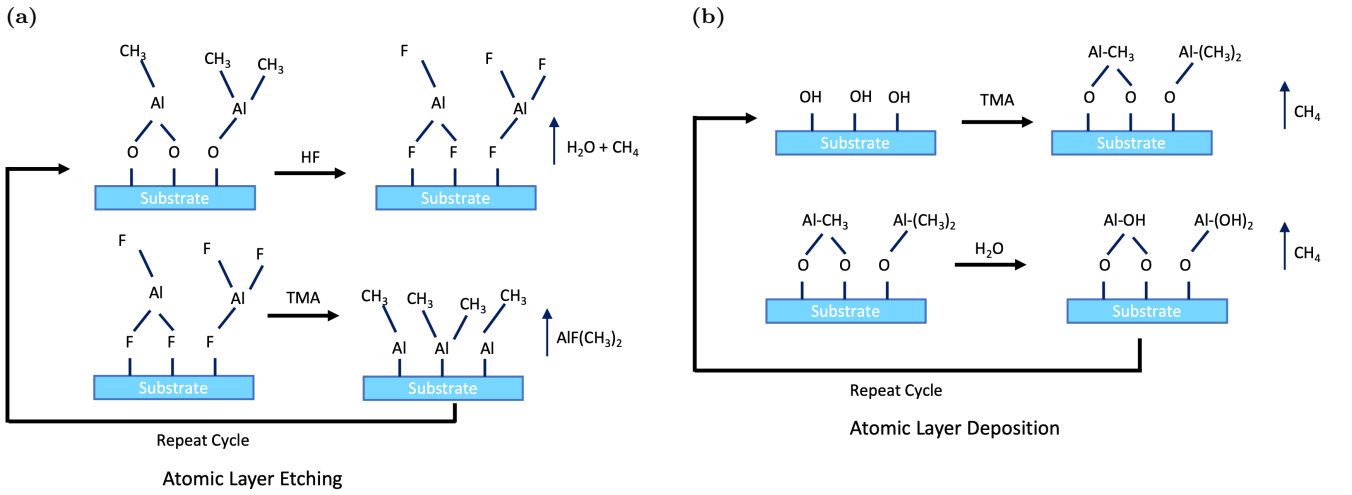

FIG. 6. Schematic representation of (a) ALE and (b) ALD using self-limiting surface chemistry and an AB binary reaction sequence.

Al_2O_3 is depicted in Figure 6(b). The proposed two-half cycle reaction can be written as follows:

$$AlOH^* + Al(CH_3)_3(g) \rightarrow AlOAl(CH_3)_2^* + CH_4(g) \uparrow \quad (4)$$

$$AlOAl(CH_3)_2^* + H_2O(g) \rightarrow AlOH^* + CH_4(g) \uparrow \quad (5)$$

The ALD surface chemistry involves formation of Al-O-$Al(CH_3)_2$ surface species during the first half cycle 'C' (equation (4)) when Al-OH* surface species react with TMA. In the second half cycle 'D' (equation (5)), these species are converted back to Al-OH* when reacted with H_2O, ultimately leading to the formation of the Al_2O_3 monolayer on the surface.

The ALD and ALE processes were developed using a Picosun/AMAT R-200 tool at 300°C. TMA (99.9999% purity from Strem) and HPLC grade water (H_2O) were used as the metal and the oxygen precursors for the Al_2O_3 ALD process while TMA and HF-pyridine (70% from Sigma Aldrich) served as the metal and fluorine sources for the etching of Al_2O_3. All the precursors were kept at room temperature. High purity nitrogen (N_2, 99.999% purity) was employed as the carrier gas to carry the precursors into the reaction chamber. The process base pressure was maintained at $\sim$ 11 hPa, with 300 sccm of N_2 directed into the chamber and $\sim$ 50 sccm of N_2 through all the precursor lines. The partial pressures of TMA, Al_2O_3 and HF-pyridine were maintained at 1.7 $\pm$ 0.2 hPa, 2.3 $\pm$ 0.2 hPa and 4 $\pm$ 0.5 hPa, respectively. N_2 was also used as a purge gas between successive doses of reactants. The optimized dosing sequence can be expressed as (t_1 - t_2 - t_3 - t_4), where t_1 is the dose time of TMA and t_3 is the dose time of H_2O or HF-pyridine, with t_2 and t_4 representing intermediate purge times. All the times are presented in seconds. The optimized dosing sequence for ALD Al_2O_3 was (0.2-10-0.2-10), while the dosing sequence for ALE Al_2O_3 was (1-10-1-10). The combined ALE+ALD process includes 50 cycles of Al_2O_3 ALE, followed by 10 cycles of Al_2O_3 ALD at 300°C. The combined recipe was applied to individual resonator and transmon chips, enabling the *in situ* removal of native Al oxide followed by encapsulation with $\sim$ 1 nm of ALD Al_2O_3 without breaking vacuum.

B. Device Fabrication

The 2D transmons and resonators were fabricated on high-resistivity silicon ($> 20\,k\Omega \cdot cm$) wafers, beginning with a 10-minute remote oxygen plasma clean at 150 W in a Tergeo asher. The first step was to deposit the Al ground layer using a lift-off process, which began with spin coating an adhesion promoter (SurPass 3000) and resist (ma-N 2403), followed by baking at 90°C, electron beam (e-beam) lithography, and development using ma-D 525. The wafers were then treated with a 10-second direct oxygen plasma exposure in an Oxford etcher and a 15-second immersion in 10:1 BOE, prior to depositing a 100-nm thick Al layer with a 10 Å/s growth rate under a base pressure of 10^{-9} Torr in an Angstrom e-beam evaporator. The lift-off process was completed by soaking the wafers in hot NMP solution at 150°C for 2 hours, followed by 5 minutes of sonication in acetone and thorough rinsing with IPA and acetone.

For the second layer (JJ), the Al ground plane was first exposed to a 5-minute remote oxygen plasma treatment in a Tergeo asher. This was followed by spin coating bilayer resists (MMA EL11 and PMMA A4 950K), with bake steps at 170°C both before and after spin coating. After e-beam lithography and cold development in a 3:1 IPA:H_2O solution at 1.6°C, the wafers underwent an O_2 plasma descum step in an Oxford etcher. They were then

exposed to a 5-minute vapor HF treatment and loaded into an Angstrom e-beam double angle evaporator within 5 minutes for junction deposition (same growth rate and base pressure as the ground layer), with deposition angles of 60° and 0°. Finally, the resist was removed with a 2-hour hot NMP treatment at 150°C, followed by 5 minutes of sonication in acetone, thorough rinsing with IPA and acetone, and a 10-minute remote oxygen plasma treatment in a Tergeo asher to remove any residual photoresist.

Scaffold oxide features were fabricated in the next step by exposing the wafers to a 10-minute remote oxygen plasma treatment in a Tergeo asher, followed by spin coating of a tri-layer resist stack (PMMA A4 950K, PMGI SF11 and ZEP 520a) with pre- and post-spin coating bake steps at 182°C. After e-beam lithography, the wafers were developed sequentially in three solutions: ZED-N50 to develop the ZEP 520a layer, MF-319 for the PMGI SF11 layer, and 3:1 IPA:H_2O mixture for the PMMA A4 layer, followed by an O_2 descum step in an Oxford etcher. A 1 μm SiO_2 layer was deposited using an Angstrom evaporator at a growth rate of 1 Å/sec and base pressure below 10^{-6} Torr. The oxide layer was lifted off in a 2-hour hot NMP treatment at 150°C, followed by rinsing with IPA and acetone and a final 10-minute remote oxygen plasma treatment in a Tergeo asher. For the Al airbridges, which form the final fabrication layer, the same process was used except that the SiO_2 deposition was replaced by *in situ* pre-deposition ion milling and deposition of a 400-nm thick Al layer in an Angstrom e-beam evaporator at a 10 Å/s growth rate and a base pressure of 10^{-9} Torr.

As a final step, the wafers underwent a 10-minute remote oxygen plasma treatment in a Tergeo asher, followed by spin coating of PMMA EL11 resist and baking at 182°C. The wafers were then diced using an ADT dicing saw, UV-cured for 7 minutes, and subsequently singulated and sorted. After dicing, the resist was removed with a 10-minute hot NMP bath at 150°C, followed by rinsing with IPA and acetone and a 10-minute remote oxygen plasma treatment in a Tergeo asher. Vapor HF treatment was used to remove the scaffold oxide, thereby releasing the airbridges and completing the fabrication. The devices were then either subjected to ALE+ALD treatment or left untreated as control samples before mounting on the PCB for wirebonding.

C. Resonator and Transmon Measurement

Measurements were conducted using a vector network analyzer (VNA) in a conventional set up to capture the S_{21} transmission of the resonators in a dilution refrigerator (DR) with a base temperature of 10 mK. The input lines consists of 75 dB total input attenuation and output line consists of a high electron mobility transistor (HEMT) amplifier at 4K stage and a room temperature amplifier.

To measure the resonator internal loss, we implemented a parameter-constrained diameter correction method (PC-DCM)[50], which reduces the parameter space in resonator data fitting and the uncertainty in the fitting result. Key parameters such as the coupling quality factor (Q_c) and impedance mismatch angle (ϕ) are extracted from high-power measurements and fixed for low-power analysis, improving fitting efficiency and robustness. For low-power measurements, we reduced the S_{21} frequency span to within one line-width of the resonance.

The quality factors reported in this study are based on measurements across three resonators on two devices for both untreated control and ALE+ALD-treated samples. The TLS-induced loss ($\delta_{\mathrm{TLS}} = \frac{1}{Q_{\mathrm{TLS}}}$) is derived from the quality factors measured at low power ($1/Q_{i,\mathrm{LP}}$, collected at 1 photon or less) and high power ($1/Q_{i,\mathrm{HP}}$) as $\delta_{\mathrm{TLS}} = \frac{1}{Q_{\mathrm{TLS}}} = \frac{1}{Q_{i,\mathrm{LP}}} - \frac{1}{Q_{i,\mathrm{HP}}}$.

Similar to the resonator measurements, transmon measurements were conducted using the same DR setup at a base temperature of 10 mK. Further details on packaging and the cryogenic setup for transmon measurements can be found elsewhere[51]. T_1 and T_2 were estimated by fitting an exponential decay to the inversion recovery[52,53] and an exponentially decaying sinusoidal to the Ramsey curve[53], respectively, with each operating point measured for at least 3 hours. The measured anharmonicity was within 10% of the design value, which is approximately 220 MHz for all transmons. Notably, the anharmonicity remained unchanged after both ALE+ALD treatment and annealing. We measured transmon decoherence at various flux points away from the sweet spot (zero flux) over a frequency range of 1.0 to 1.5 GHz from the design value. While the designed qubit frequencies were initially between 4 and 5.5 GHz, factors such as junction energy mis-targeting due to fabrication variabilities, high-temperature annealing effects, and T_1 measurements taken off the sweet spot shifted the qubit frequencies to 2.5–5 GHz.

D. Materials Characterization

The XPS measurements were performed using a Scienta Omicron instrument, with a 300 W Al X-ray source (1486.6 eV) and a base pressure of 10^{-10} mbar. The analysis area was $\sim$ 400 μm, and photoelectrons were collected at normal take-off angle. The acquired spectra were energy calibrated using the C 1s peak at $\sim$ 284.5 eV.

PiFM measurements were performed in ambient conditions using a VistaScope (Molecular Vista Inc.) system, coupled with a LaserTune QCL. The system covered an infrared spectral range from 760 to 1800 cm^{-1} with a spectral resolution of 4 cm^{-1}.

The morphology, surface oxide thickness, and elemental distribution at the Al and Si interfaces in the res-

onator and junction areas of our transmon devices, both untreated and ALE+ALD treated, were imaged using STEM-EELS. Samples were prepared via a focused ion beam (FIB) lift-out technique, using spin-on polymer (SOP) and electron-beam deposited platinum (e-Pt) before milling. The lamella thickness was ~ 70 nm. Measurements were performed on an FEI probe-corrected TITAN operated at 200 kV, in bright-field STEM and Z-contrast high-angle annular dark-field (HAADF) STEM modes, achieving a resolution of ~ 0.78 Å.

V. ACKNOWLEDGEMENTS

We thank the staff from across the AWS Center for Quantum Computing (CQC) that enabled this project. We also thank Simone Severini and Peter DeSantis for their support of the research activities at the CQC.

* Corresponding email address: mahuli@amazon.com
† Current affiliation: Google Research
‡ Current affiliation: National Institute of Standards and Technology
§ Corresponding email address: jarrige@amazon.com

[1] G. Wendin, "Quantum information processing with superconducting circuits: a review," Reports on Progress in Physics, vol. 80, no. 10, p. 106001, 2017.
[2] J. Wenner, R. Barends, R. C. Bialczak, Y. Chen, J. Kelly, E. Lucero, M. Mariantoni, A. Megrant, P. J. J. O'Malley, D. Sank, et al., "Surface loss simulations of superconducting coplanar waveguide resonators," Applied Physics Letters, vol. 99, no. 11, 2011.
[3] C. Wang, C. Axline, Y. Y. Gao, T. Brecht, Y. Chu, L. Frunzio, M. H. Devoret, and R. J. Schoelkopf, "Surface participation and dielectric loss in superconducting qubits," Applied Physics Letters, vol. 107, no. 16, 2015.
[4] J. M. Gambetta, C. E. Murray, Y.-K.-K. Fung, D. T. McClure, O. Dial, W. Shanks, J. W. Sleight, and M. Steffen, "Investigating surface loss effects in superconducting transmon qubits," IEEE Transactions on Applied Superconductivity, vol. 27, no. 1, pp. 1–5, 2016.
[5] M. D. Reed, B. R. Johnson, A. A. Houck, L. DiCarlo, J. M. Chow, D. I. Schuster, L. Frunzio, and R. J. Schoelkopf, "Fast reset and suppressing spontaneous emission of a superconducting qubit," Applied Physics Letters, vol. 96, no. 20, 2010.
[6] E. Jeffrey, D. Sank, J. Y. Mutus, T. C. White, J. Kelly, R. Barends, Y. Chen, Z. Chen, B. Chiaro, A. Dunsworth, et al., "Fast accurate state measurement with superconducting qubits," Physical review letters, vol. 112, no. 19, p. 190504, 2014.
[7] C. E. Murray, "Material matters in superconducting qubits," Materials Science and Engineering: R: Reports, vol. 146, p. 100646, 2021.
[8] A. P. M. Place, L. V. H. Rodgers, P. Mundada, B. M. Smitham, M. Fitzpatrick, Z. Leng, A. Premkumar, J. Bryon, A. Vrajitoarea, S. Sussman, et al., "New material platform for superconducting transmon qubits with coherence times exceeding 0.3 milliseconds," Nature communications, vol. 12, no. 1, p. 1779, 2021.
[9] M. P. Bland, F. Bahrami, J. G. C. Martinez, P. H. Prestegaard, B. M. Smitham, A. Joshi, E. Hedrick, A. Pakpour-Tabrizi, S. Kumar, A. Jindal, et al., "2D transmons with lifetimes and coherence times exceeding 1 millisecond," arXiv preprint arXiv:2503.14798, 2025.
[10] W. Woods, G. Calusine, A. Melville, A. Sevi, E. Golden, D. K. Kim, D. Rosenberg, J. L. Yoder, and W. D. Oliver, "Determining interface dielectric losses in superconducting coplanar-waveguide resonators," Physical Review Applied, vol. 12, no. 1, p. 014012, 2019.
[11] M. V. P. Altoé, A. Banerjee, C. Berk, A. Hajr, A. Schwartzberg, C. Song, M. Alghadeer, S. Aloni, M. J. Elowson, J. M. Kreikebaum, et al., "Localization and mitigation of loss in niobium superconducting circuits," PRX Quantum, vol. 3, no. 2, p. 020312, 2022.
[12] K. D. Crowley, R. A. McLellan, A. Dutta, N. Shumiya, A. P. M. Place, X. H. Le, Y. Gang, T. Madhavan, M. P. Bland, R. Chang, et al., "Disentangling losses in tantalum superconducting circuits," Physical Review X, vol. 13, no. 4, p. 041005, 2023.
[13] C. J. Kopas, D. P. Goronzy, T. Pham, C. G. Torres Castanedo, M. Cheng, R. Cochrane, P. Nast, E. Lachman, N. Z. Zhelev, A. Vallières, et al., "Enhanced superconducting qubit performance through ammonium fluoride etch," Materials for Quantum Technology, 2024.
[14] D. P. Lozano, M. Mongillo, X. Piao, S. Couet, D. Wan, Y. Canvel, A. M. Vadiraj, T. Ivanov, J. Verjauw, R. Acharya, et al., "Low-loss α-tantalum coplanar waveguide resonators on silicon wafers: fabrication, characterization and surface modification," Materials for Quantum Technology, vol. 4, no. 2, p. 025801, 2024.
[15] C. Zhou, J. Mun, J. Yao, A. k. Anbalagan, M. D. Hossain, R. A. McLellan, R. Li, K. Kisslinger, G. Li, X. Tong, et al., "Ultrathin magnesium-based coating as an efficient oxygen barrier for superconducting circuit materials," Advanced Materials, vol. 36, no. 18, p. 2310280, 2024.
[16] M. Bal, A. A. Murthy, S. Zhu, F. Crisa, X. You, Z. Huang, T. Roy, J. Lee, D. v. Zanten, R. Pilipenko, et al., "Systematic improvements in transmon qubit coherence enabled by niobium surface encapsulation," npj Quantum Information, vol. 10, no. 1, p. 43, 2024.
[17] S. K. Karuppannan, D. Huang, N. M. Kommanaboina, K. Anil, G. Yan, D. V. M. Repaka, Y. Zhang, K. E. J. Goh, W. S. Kai, N. L. C. Beng, et al., "Improved interface of niobium superconducting resonator with ruthenium as a capping layer," ACS Applied Electronic Materials, 2024.
[18] R. D. Chang, N. Shumiya, R. A. McLellan, Y. Zhang, M. P. Bland, F. Bahrami, J. Mun, C. Zhou, K. Kisslinger, G. Cheng, et al., "Eliminating surface oxides of superconducting circuits with noble metal encapsulation," Physical review letters, vol. 134, no. 9, p. 097001, 2025.
[19] C. R. H. McRae, H. Wang, J. Gao, M. R. Vissers, T. Brecht, A. Dunsworth, D. P. Pappas, and J. Mutus, "Materials loss measurements using superconducting microwave resonators," Review of Scientific Instruments, vol. 91, no. 9, 2020.

[20] G. Marcaud, D. Perello, C. Chen, E. Umbarkar, C. Weiland, J. Gao, S. Diez, V. Ly, N. Mahuli, N. D'Souza, et al., "Low-loss superconducting resonators fabricated from tantalum films grown at room temperature," arXiv preprint arXiv:2501.09885, 2025.

[21] Q.-M. Chen, M. Pfeiffer, M. Partanen, F. Fesquet, K. E. Honasoge, F. Kronowetter, Y. Nojiri, M. Renger, K. G. Fedorov, A. Marx, et al., "Scattering coefficients of superconducting microwave resonators. i. transfer matrix approach," Physical Review B, vol. 106, no. 21, p. 214505, 2022.

[22] P. G. Baity, C. Maclean, V. Seferai, J. Bronstein, Y. Shu, T. Hemakumara, and M. Weides, "Circle fit optimization for resonator quality factor measurements: Point redistribution for maximal accuracy," Physical Review Research, vol. 6, no. 1, p. 013329, 2024.

[23] G. Calusine, A. Melville, W. Woods, R. Das, C. Stull, V. Bolkhovsky, D. Braje, D. Hover, D. K. Kim, X. Miloshi, et al., "Analysis and mitigation of interface losses in trenched superconducting coplanar waveguide resonators," Applied Physics Letters, vol. 112, no. 6, 2018.

[24] R. Barends, J. Kelly, A. Megrant, D. Sank, E. Jeffrey, Y. Chen, Y. Yin, B. Chiaro, J. Mutus, C. Neill, et al., "Coherent josephson qubit suitable for scalable quantum integrated circuits," Physical review letters, vol. 111, no. 8, p. 080502, 2013.

[25] P. V. Klimov, J. Kelly, Z. Chen, M. Neeley, A. Megrant, B. Burkett, R. Barends, K. Arya, B. Chiaro, Y. Chen, et al., "Fluctuations of energy-relaxation times in superconducting qubits," Physical review letters, vol. 121, no. 9, p. 090502, 2018.

[26] C. C Yu and H. M. Carruzzo, "Two-level systems and the tunneling model: A critical view," Low-temperature Thermal And Vibrational Properties Of Disordered Solids: A Half-century Of Universal" Anomalies" Of Glasses, p. 113, 2022.

[27] Y. Lee, J. W. DuMont, and S. M. George, "Trimethylaluminum as the metal precursor for the atomic layer etching of Al_2O_3 using sequential, self-limiting thermal reactions," Chemistry of Materials, vol. 28, no. 9, pp. 2994–3003, 2016.

[28] R. L. Puurunen, "Surface chemistry of atomic layer deposition: A case study for the trimethylaluminum/water process," Journal of applied physics, vol. 97, no. 12, 2005.

[29] S. Prasanna, G. Krishnendu, S. Shalini, P. Biji, G. M. Rao, S. Jayakumar, and R. Balasundaraprabhu, "Composition, structure and electrical properties of DC reactive magnetron sputtered Al_2O_3 thin films," Materials science in semiconductor processing, vol. 16, no. 3, pp. 705–711, 2013.

[30] N. Reddy, P. Bera, V. R. Reddy, N. Sridhara, A. Dey, C. Anandan, and A. K. Sharma, "XPS study of sputtered alumina thin films," Ceramics International, vol. 40, no. 7, pp. 11099–11107, 2014.

[31] G. A. Mengesha, J. P. Chu, B.-S. Lou, and J.-W. Lee, "Corrosion performance of plasma electrolytic oxidation grown oxide coating on pure aluminum: effect of borax concentration," Journal of Materials Research and Technology, vol. 9, no. 4, pp. 8766–8779, 2020.

[32] L. Nguyen, T. Hashimoto, D. N. Zakharov, E. A. Stach, A. P. Rooney, B. Berkels, G. E. Thompson, S. J. Haigh, and T. L. Burnett, "Atomic-scale insights into the oxidation of aluminum," ACS applied materials & interfaces, vol. 10, no. 3, pp. 2230–2235, 2018.

[33] G. Duan, C. Zhang, A. Li, X. Yang, L. Lu, and X. Wang, "Preparation and characterization of mesoporous zirconia made by using a poly (methyl methacrylate) template," Nanoscale research letters, vol. 3, pp. 118–122, 2008.

[34] S. B. Aziz, O. G. Abdullah, M. Brza, A. K. Azawy, and D. A. Tahir, "Effect of carbon nano-dots (CNDs) on structural and optical properties of PMMA polymer composite," Results in Physics, vol. 15, p. 102776, 2019.

[35] D. N. Goldstein, J. A. McCormick, and S. M. George, "Al_2O_3 atomic layer deposition with trimethylaluminum and ozone studied by *in situ* transmission FTIR spectroscopy and quadrupole mass spectrometry," The Journal of Physical Chemistry C, vol. 112, no. 49, pp. 19530–19539, 2008.

[36] V. Vemuri, S. W. King, W. A. Lanford, J. T. Gaskins, P. E. Hopkins, J. Van Derslice, H. Li, and N. C. Strandwitz, "Comprehensive study of the chemical, physical, and structural evolution of molecular layer deposited alucone films during thermal processing," Chemistry of Materials, vol. 35, no. 5, pp. 1916–1925, 2023.

[37] T. Kashiwagi, A. Inabi, and A. Hamins, "Behavior of primary radicals during thermal degradation of poly (methyl methacrylate)," Polymer Degradation and Stability, vol. 26, no. 2, pp. 161–184, 1989.

[38] L. E. Manring, "Thermal degradation of poly (methyl methacrylate). 4. random side-group scission," Macromolecules, vol. 24, no. 11, pp. 3304–3309, 1991.

[39] H. A. Al-Abadleh and V. Grassian, "FT-IR study of water adsorption on aluminum oxide surfaces," Langmuir, vol. 19, no. 2, pp. 341–347, 2003.

[40] Y. Lee, J. W. DuMont, A. S. Cavanagh, and S. M. George, "Atomic layer deposition of AlF_3 using trimethylaluminum and hydrogen fluoride," The Journal of Physical Chemistry C, vol. 119, no. 25, pp. 14185–14194, 2015.

[41] J. W. DuMont and S. M. George, "Competition between Al_2O_3 atomic layer etching and AlF_3 atomic layer deposition using sequential exposures of trimethylaluminum and hydrogen fluoride," The Journal of Chemical Physics, vol. 146, no. 5, 2017.

[42] G. P. Gakis, H. Vergnes, F. Cristiano, Y. Tison, C. Vahlas, B. Caussat, A. G. Boudouvis, and E. Scheid, "*In situ* N_2-NH_3 plasma pre-treatment of silicon substrate enhances the initial growth and restricts the substrate oxidation during alumina ALD," Journal of Applied Physics, vol. 126, no. 12, 2019.

[43] W. Xu, R. J. Gasvoda, P. C. Lemaire, K. Sharma, D. M. Hausmann, and S. Agarwal, "Area-selective atomic layer deposition of Al_2O_3 on SiN_x with SiO_2 as the nongrowth surface," Journal of Vacuum Science & Technology A, vol. 40, no. 1, 2022.

[44] W. Xu, P. C. Lemaire, K. Sharma, D. M. Hausmann, and S. Agarwal, "Extending growth inhibition during area-selective atomic layer deposition of Al_2O_3 on aminosilane-functionalized SiO_2," Chemical Communications, vol. 58, no. 46, pp. 6650–6652, 2022.

[45] E. Papirer, J.-M. Perrin, G. Nanse, and P. Fioux, "Adsorption of poly (methylmethacrylate) on an α alumina: evidence of formation of surface carboxylate bonds," European polymer journal, vol. 30, no. 8, pp. 985–991, 1994.

[46] J. F. Watts, S. R. Leadley, J. E. Castle, and C. J. Blomfield, "Adsorption of PMMA on oxidized Al and Si substrates: An investigation by high-resolution X-ray photo-

electron spectroscopy," Langmuir, vol. 16, no. 5, pp. 2292–2300, 2000.

[47] M. Ferriol, A. Gentilhomme, M. Cochez, N. Oget, and J. L. Mieloszynski, "Thermal degradation of poly (methyl methacrylate)(PMMA): modelling of DTG and TG curves," Polymer degradation and stability, vol. 79, no. 2, pp. 271–281, 2003.

[48] M. Almajhadi and H. K. Wickramasinghe, "Contrast and imaging performance in photo induced force microscopy," Optics Express, vol. 25, no. 22, pp. 26923–26938, 2017.

[49] R. A. McLellan, A. Dutta, C. Zhou, Y. Jia, C. Weiland, X. Gui, A. P. M. Place, K. D. Crowley, X. H. Le, T. Madhavan, et al., "Chemical profiles of the oxides on tantalum in state of the art superconducting circuits," Advanced Science, vol. 10, no. 21, p. 2300921, 2023.

[50] C. Chen, D. Perello, S. Aghaeimeibodi, G. Marcaud, I. Jarrige, H. Lee, W. Fon, M. Matheny, and J. Gao, "Efficient methods for extracting superconducting resonator loss in the single-photon regime," Journal of Applied Physics, vol. 137, no. 4, 2025.

[51] H. Levine, A. Haim, J. S. C. Hung, N. Alidoust, M. Kalaee, L. DeLorenzo, E. A. Wollack, P. Arrangoiz-Arriola, A. Khalajhedayati, R. Sanil, et al., "Demonstrating a long-coherence dual-rail erasure qubit using tunable transmons," Physical Review X, vol. 14, no. 1, p. 011051, 2024.

[52] Z. Wei, Y.-J. Ma, H. Jang, W. Yang, and J. Du, "To measure T_1 of short T_2 species using an inversion recovery prepared three-dimensional ultrashort echo time (3D IR-UTE) method: A phantom study," Journal of Magnetic Resonance, vol. 314, p. 106725, 2020.

[53] J. A. Montañez-Barrera, M. R. von Spakovsky, C. E. Damian Ascencio, and S. Cano-Andrade, "Decoherence predictions in a superconducting quantum processor using the steepest-entropy-ascent quantum thermodynamics framework," Physical Review A, vol. 106, no. 3, p. 032426, 2022.

SUPPLEMENTARY INFORMATION FOR "IMPROVING THE LIFETIME OF ALUMINUM-BASED SUPERCONDUCTING QUBITS THROUGH ATOMIC LAYER ETCHING AND DEPOSITION"

OUTLINE

I. TRANSMON DESIGN AND MEASUREMENT PARAMETERS

Five different chips, each containing four tunable transmons (Q1-Q4), were measured in the frequency range of 2.2–4.4 GHz before and after the treatment along with six additional untreated chips. One chip was also measured before and after annealing at 300°C under vacuum in the ALD chamber. All these chips came from two different wafers fabricated with the same process flow. A micrograph of a transmon is shown in Figure SI-1(a). Design and measurement parameters are summarized in the table in Figure SI-1(b).

(a)

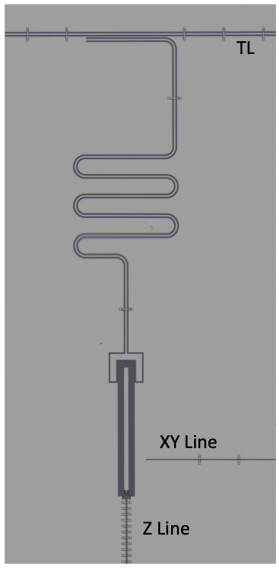

(b)

Parameter	Q1	Q2	Q3	Q4
Measurement f_{01} range (GHz)	2.3-3.9	2.6-4.4	2.4-4.3	2.9-4.9
Readout resonator frequency (GHz)	5.55	6.4	5.8	6.56
JJ length (nm)	200	200	200	200
JJ width (nm)	163	200	157	286
Capacitor width (um)	24	24	24	24
Capacitor gap (um)	30	30	30	30
Capacitor length (um)	684.2	684.2	645	631
Coupling strength (g) (MHz)	59.7	78.4	60.6	61.1
Coupling capacitance (C_g) (fF)	5.6	6.23	5.27	4.32
Qubit capacitance (C_q) (fF)	87.1	87.1	86.3	84.7

FIG. SI-1. (a) Optical micrograph of a transmon device and (b) Summary of transmon design and measurement parameters

II. CALCULATED PURCELL CURVES AND MEASURED Q FOR INDIVIDUAL TRANSMONS

After the ALE+ALD treatment, we consistently observed a positive frequency shift across all transmon designs. As a consequence of this frequency shift, the readout resonator Purcell loss was enhanced at the maximum f_{01} transmon transition frequency. The increase in f_{01} contributed to the Purcell effect, which may have been a key factor behind the observed tapering of the transmon performance at higher frequencies. To investigate this behavior further, we calculated the Purcell curves for all four transmon designs using the experimentally determined resonator coupling rate (κ_c) limits. The Purcell curves (as shown in Figure SI-2) were calculated using the following formula: The decay time T_P is given by:

$$T_P = \frac{2\pi}{\kappa_c} \cdot \left(\frac{g f_r - f_{01}}{f_r} \right)^2 \tag{6}$$

where,

T_P is the Purcell-limited decay time of the qubit — the rate at which the qubit loses energy due to coupling to the readout resonator,

κ_c is the resonator coupling rate (external linewidth), typically defined as $\kappa_c = \omega_r / Q_c$, where Q_c is the coupling quality factor, and ω_r is the angular resonance frequency,

g is the qubit-resonator coupling strength, describing the strength of interaction between the two systems,

f_r is the resonator frequency,

f_{01} is the qubit transition frequency, corresponding to the energy difference between the ground and first excited state.

The coupling g is defined as:

$$g = \frac{2\pi f_r f_{01}}{C_{qu} C_{rr}} \cdot \frac{C_{qu} - C_{rr}}{C_{qu-rr}} \tag{7}$$

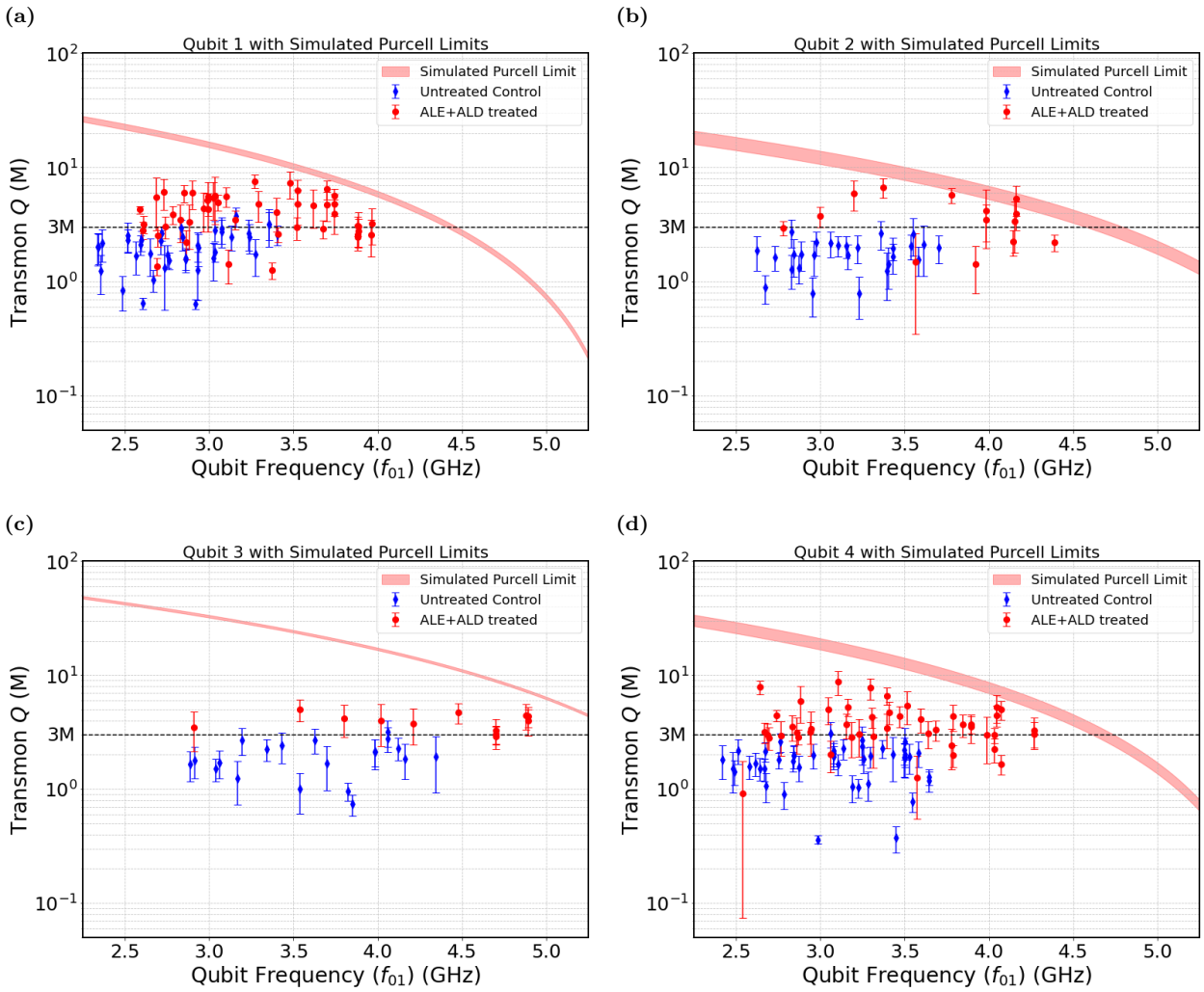

FIG. SI-2. Frequency dependence of the estimated Q for each qubit design, for various untreated and ALE+ALD treated devices, along with their calculated Purcell curves based on experimentally measured upper and lower limits of κ_c.

where,

C_{qu} is the total qubit capacitance,

C_{rr} is the total resonator capacitance,

C_{qu-rr} is the coupling capacitance between the qubit and resonator,

$2\pi f_r f_{01}$ arises from quantization of the circuit Hamiltonian and reflects the energy exchange rate between the systems.

The Purcell-limited quality factor Q_P is given by:

$$Q_P = \frac{2\pi f_{01}}{T_P} \tag{8}$$

As suggested by the plots in Figure SI-2, the readout Purcell loss appears to contribute to loss for all four transmon designs near their maximum f_{01} frequency. In future studies, we plan to investigate fabrication methods to minimize treatment-induced shifts of the transmon frequency toward the readout frequency, thereby reducing the Purcell loss in our devices.

III. FREQUENCY SHIFT AFTER ALE+ALD TREATMENT FOR INDIVIDUAL TRANSMONS

As shown in Figure SI-3, an upward frequency shift of +500-800 MHz is consistently observed post ALE+ALD across all studied transmon designs, independent of their untreated starting frequencies or source wafer. While we attribute this positive frequency shift to the high processing temperatures of ALE and ALD, the exact magnitude of this shift may be influenced by additional factors, including fabrication process variations and differences in residual polymeric contamination on the surface prior to treatment.

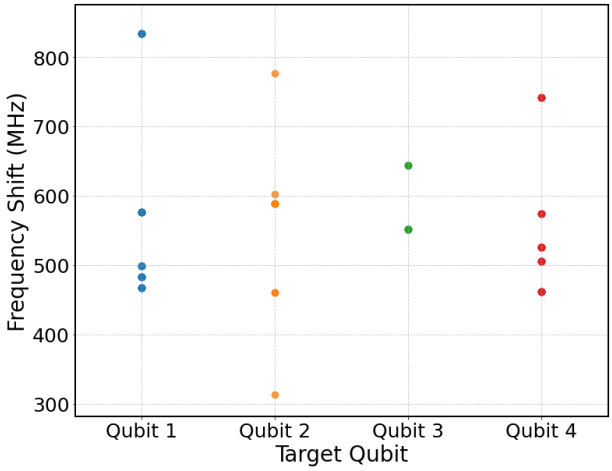

FIG. SI-3. Measured upward frequency shift after ALE+ALD treatment on individual transmon designs, showing a consistent increase of 500-800 MHz, irrespective of the untreated transmon frequency.

IV. TRANSMON Q DEPENDENCE AS A FUNCTION OF FREQUENCY SHIFT AFTER ALE+ALD TREATMENT

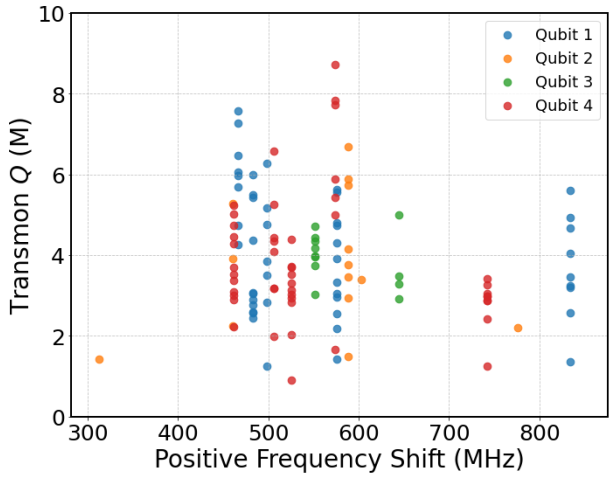

FIG. SI-4. Measured dependence of transmon Q on the absolute frequency shift for various ALE+ALD treated devices.

We observe a noticeable correlation between frequency shift and transmon quality factor Q, where the median transmon Q decreases with increasing frequency shift, as shown in Figure SI-4. This behavior is attributed to enhanced readout Purcell loss as the transmon f_{01} approaches the readout frequency, as discussed in Section II of the SI. Specifically, the median transmon Q decreases from approximately 4–6x10^6 for frequency shifts of 450 MHz to about 2–3x10^6 for shifts above 700 MHz.

V. XPS PEAK FITTING

Surface analysis was conducted on four samples using x-ray photoelectron spectroscopy (XPS): as-deposited blanket Al film, untreated device, ALE+ALD treated device, and annealed-only device. Experimental spectra for the Al $2p$, C $1s$, and O $1s$ core levels were individually curve-fitted after subtracting a Shirley background using CasaXPS.

A symmetric Voigt function was used for all the three components in the curve-fitting of the C $1s$ spectrum (Figure SI-5), which reveals peaks at $\sim$ 284.5 eV corresponding to -C-C- and -C-H- bonds from adventitious carbon, $\sim$ 285.5 eV for -C-OH- and -C-O-C- species; and $\sim$ 288.5 eV for -O=C-O- functional groups associated with surface oxidation or contamination. The Al $2p$ core-level spectra (Figure SI-6) were analyzed with a symmetric Voigt function for oxides and a Lorentzian asymmetric function for metallic Al. The metallic doublet positions were constrained within 0.44 eV with a 2:1 area ratio for Al $2p_{3/2}$ and Al $2p_{1/2}$. A single oxide component was identified in the as-deposited Al film and ALE+ALD treated device, while an additional peak around 75.6 eV (-Al-O-OH-) appeared due to organic or polymeric contamination in the annealed-only and untreated devices. A shift of the Al oxide component for the annealed-only and untreated devices towards higher binding energies suggests the formation of oxygen-rich AlO_x. The deconvolution of the O $1s$ core-level spectra (Figure SI-7) using symmetric Voigt functions reveals the presence of three components: $\sim$ 530.7 eV for Al-O-Al bonding, $\sim$ 531.8 eV for -OH or Al-O-OH species, and $\sim$ 533 eV for adsorbed H_2O.

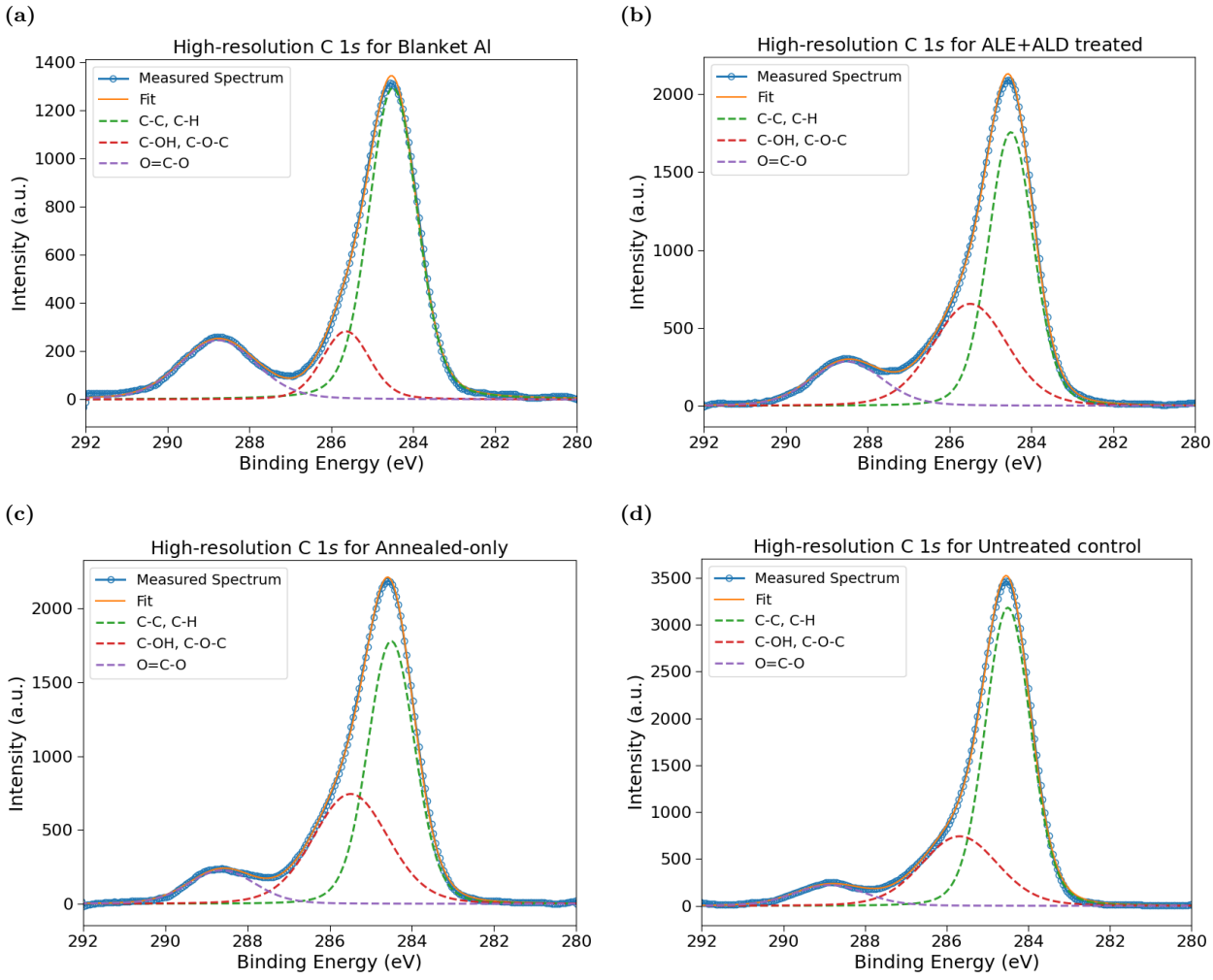

FIG. SI-5. C $1s$ core-level XPS spectra of (a) as-deposited blanket Al film, (b) ALE+ALD treated device, (c) annealed-only device, and (d) untreated device.

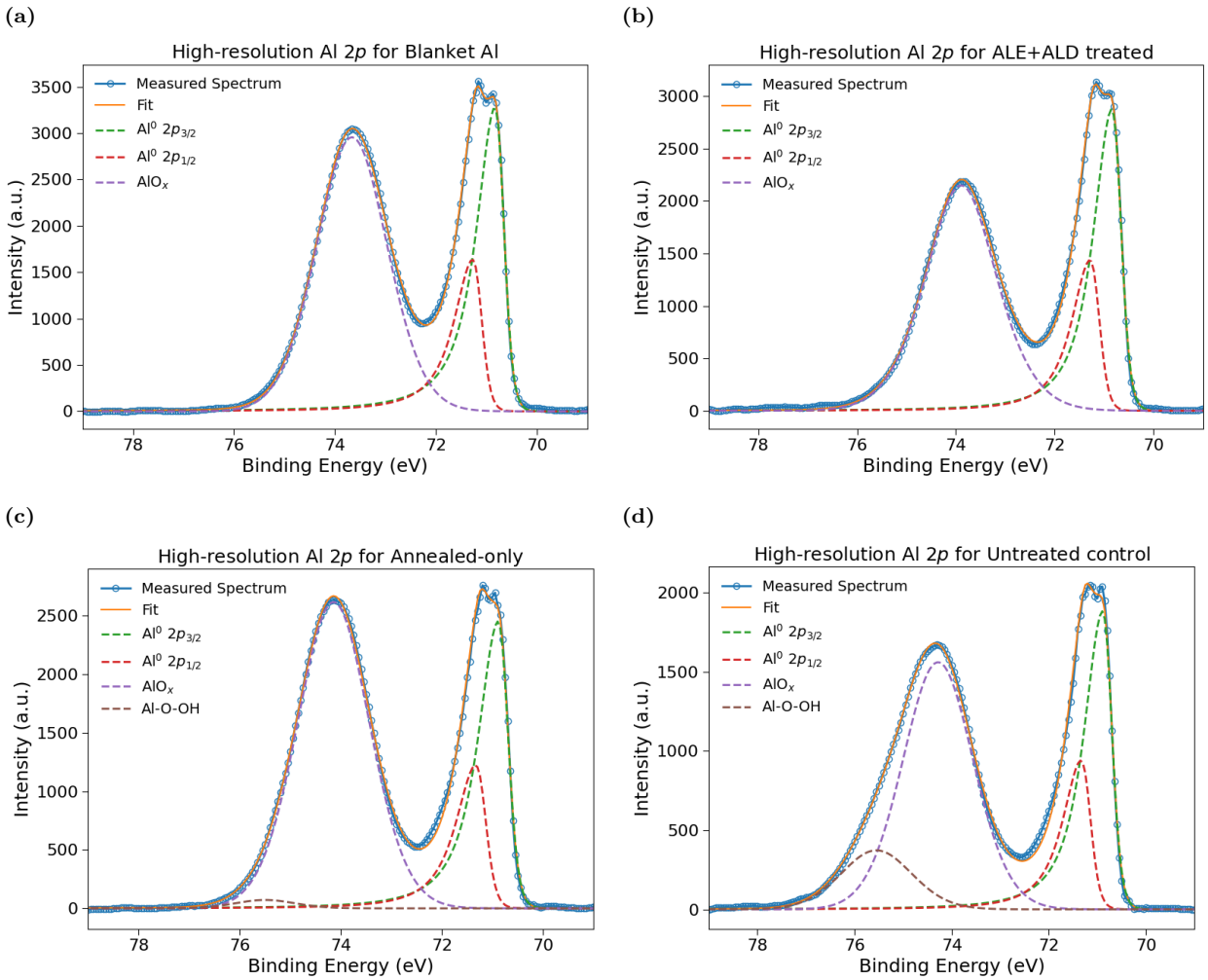

FIG. SI-6. Al 2p core-level XPS spectra of (a) as-deposited blanket Al film, (b) ALE+ALD treated device, (c) annealed-only device, and (d) untreated device.

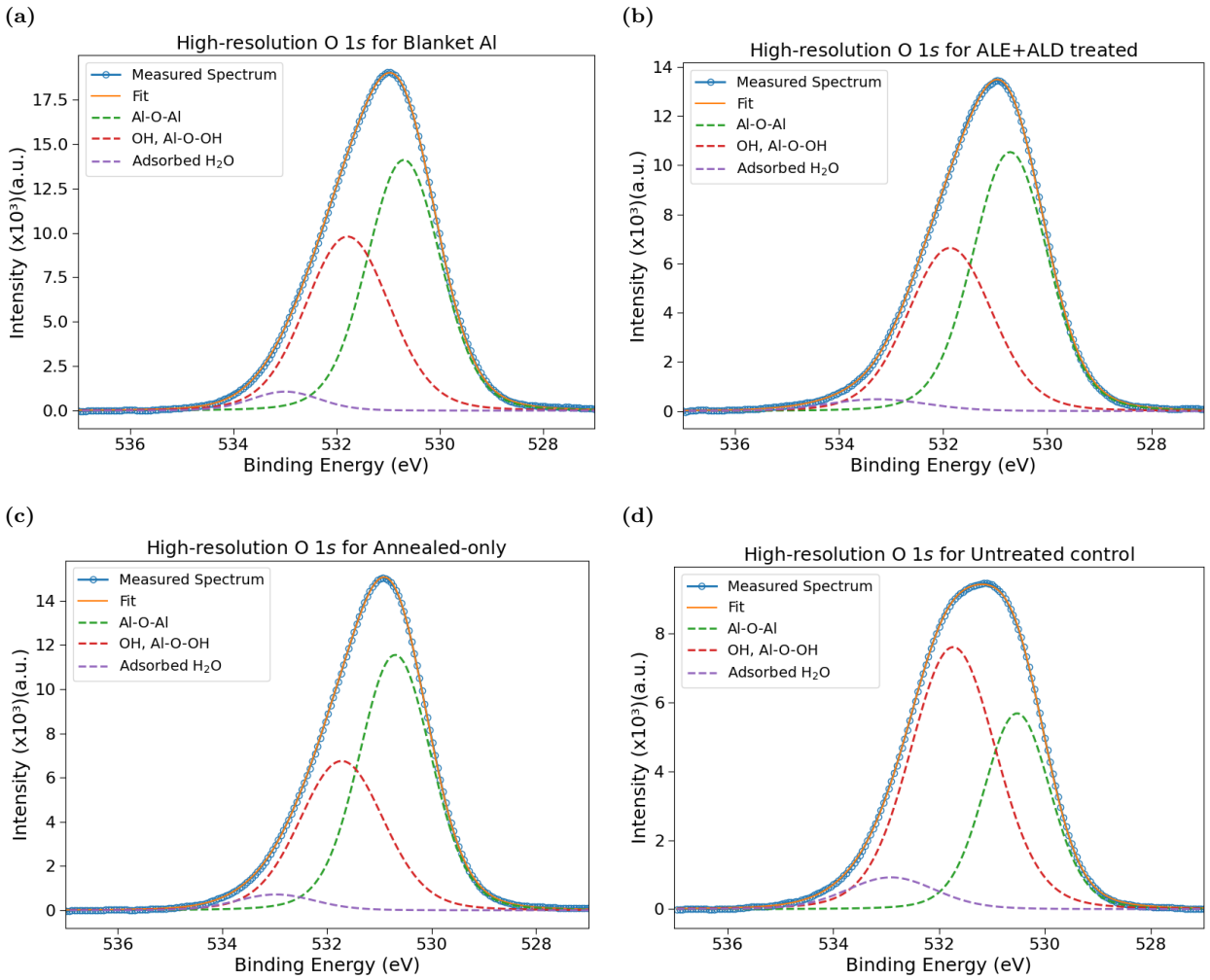

FIG. SI-7. O 1*s* core-level XPS spectra of (a) as-deposited blanket Al film, (b) ALE+ALD treated device, (c) annealed-only device, and (d) untreated device.

VI. ESTIMATION OF AL_2O_3 THICKNESS FROM XPS ANALYSIS

The thickness of the Al_2O_3 layer was estimated based on the intensity ratio of the Al 2*p* peaks respectively corresponding to the oxide and the underlying metal in the experimental spectra. This method is based on the attenuation of photoelectrons emitted from the metal substrate as they pass through the oxide layer. The thickness d of the Al_2O_3 layer can be inferred using the following equation based on the Beer-Lambert Law:

$$d_{xps}(\text{Å}) = \lambda_0 \sin\theta \cdot \ln\left(\frac{N_m\lambda_m}{N_0\lambda_0} \cdot \frac{I_0}{I_m} + 1\right)$$

where,
d = thickness of the Al_2O_3 layer
λ_0 = inelastic mean free path (IMFP) of Al 2*p* electrons in Al_2O_3
λ_m = IMFP of Al 2*p* electrons in metallic Al
θ = take off angle
I_m = XPS intensity of metallic Al 2*p* peak
I_0 = XPS intensity of oxidized Al 2*p* peak
N_m = Atomic density of metallic Al
N_0 = Atomic density of metallic Al_2O_3

The XPS intensity was determined from the total area under the curve of the Al $2p$ core level for the metallic and oxide components. Using the above equation with a take-off angle of 90 degrees, and λ_0 and λ_m values of 28 $\mathring{A}$ and 26 $\mathring{A}$ for Al oxide and Al metal, respectively, along with an N_m:N_0 ratio of 1.5, the thickness was estimated for different samples and several locations on each chip as shown in Figure 3(b) of the main text.

VII. TEM-EELS ANALYSIS

We performed imaging of the JJ and resonator areas to study the surface oxide layers using transmission electron microscopy and electron energy loss spectroscopy (TEM-EELS), as shown in Figure SI-8(a-d). The thicknesses of the surface Al oxide layers were found to be consistent with XPS estimations: 2.5 ± 0.2 nm for the ALE+ALD treated chip and in the 3.1 ± 0.2 nm for the untreated chip. This confirms a measurable reduction in the oxide layer thickness of the treated chip, and underscores the uniformity of the treatment's effect on the surface oxide layer. The oxide thickness was estimated by averaging measurements from 25 locations across all the images shown in Figure SI-8 using the software ImageJ. For each chip, the O/Al ratio was also estimated based on an EELS map collected across the surface oxide layer. This ratio was estimated to be approximately 1.5 for both chips, suggesting that the differences in oxidation state identified via XPS are either too small to be detected just by TEM-EELS spectral mapping alone or have been further minimized by the lamella preparation process used for TEM. Additionally, EELS maps (Figure SI-8(e)) measured on exposed Si areas next to the resonators indicate that the native silicon oxide is not capped by Al_2O_3, which is consistent with the PiFM data.

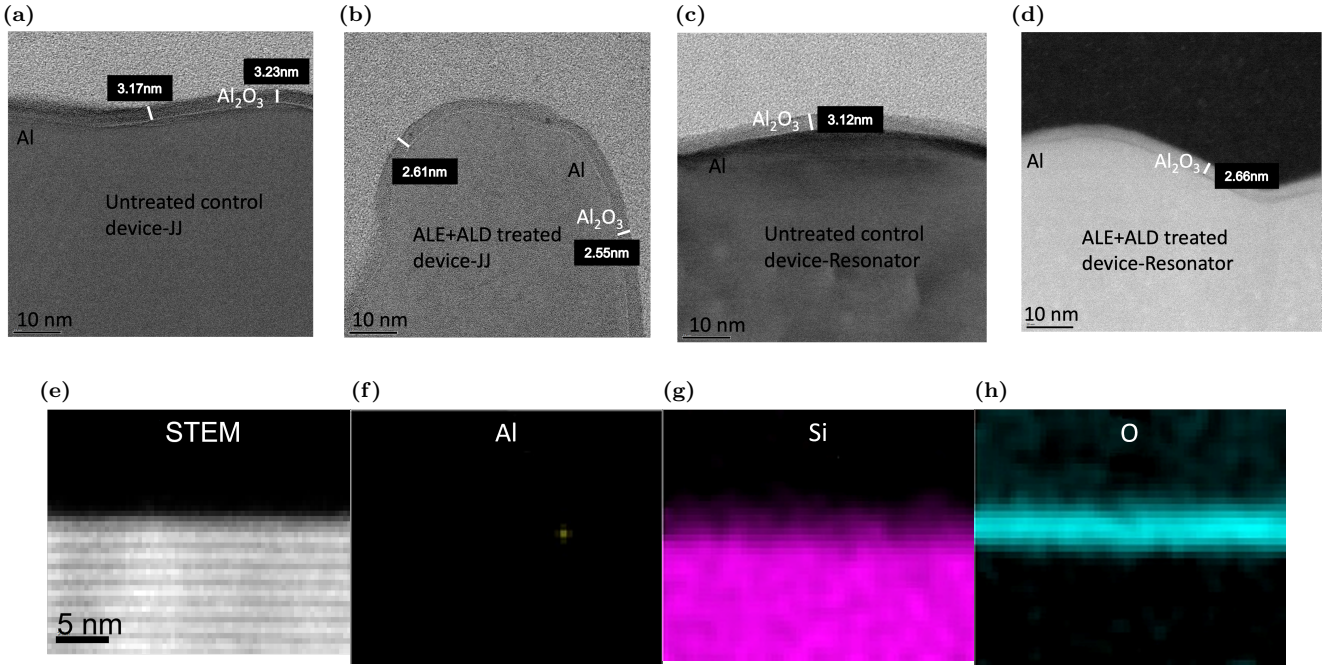

FIG. SI-8. (a-d) High-resolution scanning-TEM images of the vicinity of the surface of the the JJ top electrode and read-out resonator trace on untreated and treated devices. (e) S-TEM image of the Si trench region in the ALE+ALD-treated resonator, alongwith TEM-EELS elemental maps for (f) Al, (g) Si and (h) O, showing the absence of detectable Al_2O_3 on the exposed Si surface.

VIII. IR PEAK ASSIGNMENT

Table I summarizes the peak assignments for all peaks identified in the Al and Si regions of the resonators and junctions on both untreated and treated surfaces.

Peak Assignment	Wavenumbers (cm^{-1})				
	Untreated		ALE+ALD Treated		
	Resonator	Junction	Resonator-Al trace	Resonator-Si trench	Junction
Al-O stretching vibration	-	-	800-1000	-	800-1000
C-O stretching vibration from PMMA	-	-	1020	1020	-
C-O-C stretching vibration from PMMA	1150	1150	-	-	-
C-H bending vibration from Al-CH_3	-	-	1167	1167	1167
C-O-C stretching vibration from PMMA	1197	1197	1197	1197	-
C-O-C stretching vibration from PMMA	1240	1240	-	-	-
C-O-C stretching vibration from PMMA	1265	1265	1265	1265	1265
CH_x bending deformation	1378	1378	1378	1378	1378
CH_x bending deformation	1445	1445	1445	1445	1445
CH_x bending deformation	1466	1466	1466	1466	1466
C=O stretching vibration from PMMA	1735	1735	1735	1735	-

TABLE I. Infrared spectra peak assignments for untreated and ALE+ALD treated devices.

IX. PIFM MAPPING OF RESONATOR AREA

In this section, we present raw PiFM maps (Figure SI-9) of the resonator area for ALE+ALD-treated devices, acquired at 912 cm^{-1} and 1171 cm^{-1}, corresponding to the Al–O stretching vibration and the C=O stretching vibration in PMMA, respectively.

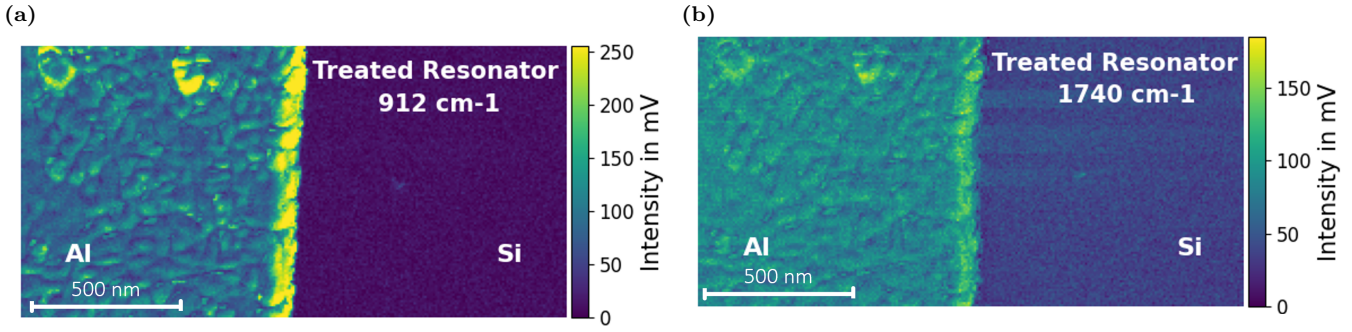

FIG. SI-9. PiFM maps at the resontor area shown with a color scale highlighting the 912 cm^{-1} and 1171 cm^{-1} wavenumbers, which respectively correspond to Al-O bonds and organic C-H bending and/or CH_3 deformation